J. Appl. Comput. Mech., xx(x) (2026) 1-14
DOI: 10.22055/jacm.2026.49003.5659

ISSN: 2383-4536
jacm.scu.ac.ir

Shahid Chamran University of Ahvaz

Journal of Applied and Computational Mechanics

Research Paper

Physics-Informed Neural Network Modeling of Corneal Inflation: Forward Prediction and Inverse Parameter Identification

Ying Zhang[1,2], Zhengwen Gao[3], Zimeng Zhou[1,2], Honghao Wang[1,2], Xiaohua Lv[1,2], Xiuli Liu[1,2], Tingwei Quan[1,2], Shaoqun Zeng[1,2]

[1] Britton Chance Center for Biomedical Photonics, Wuhan National Laboratory for Optoelectronics, Huazhong University of Science and Technology, Wuhan, Hubei, 430074, China

[2] MOE Key Laboratory for Biomedical Photonics, Wuhan National Laboratory for Optoelectronics, Huazhong University of Science and Technology, Wuhan 430074, China

[3] College of Life Science and Technology, Huazhong University of Science and Technology, Wuhan, Hubei, 430074, China

Received December 15 2025; Revised March 16 2026; Accepted for publication March 19 2026.
✉ Corresponding authors: H. Wang (wanghonghao@hust.edu.cn); S. Zeng (sqzeng@hust.edu.cn)

Abstract. The cornea is vital for the eye's optical function and structural integrity, with its biomechanics regulating intraocular pressure (IOP), preserving vision, and ensuring safe, effective refractive surgeries. Corneal inflation experiments serve as a vital approach to investigate the mechanical behavior of the cornea under physiological IOP by measuring displacement responses at varying pressure levels, thus providing key data that reflect its biomechanical characteristics. Accurate forward prediction of mechanical responses and inverse identification of mechanical parameters in these experiments are of significant value for the quantitative assessment of corneal biomechanics. In recent years, Physics-Informed Neural Networks (PINNs), an emerging approach that integrates physical prior knowledge with deep learning, have demonstrated strong capabilities in solving partial differential equations (PDEs). Based on the PINN framework, this study investigates forward mechanical response prediction and inverse parameter identification in corneal inflation experiments. Experimental validation using Polydimethylsiloxane (PDMS) artificial corneas demonstrated that the proposed method performs well in both forward prediction and inverse identification tasks, and its effectiveness was confirmed through comparison with the finite element method. This study provides an innovative solution for biomechanical modeling and material parameter identification in corneal inflation experiments.

Keywords: Cornea, Biomechanics, Inflation experiment, Physics-informed neural networks, Finite element method.

1. Introduction

Cornea plays a critical role in maintaining the normal optical performance and structural stability of the eye. Its biomechanical properties are essential for regulating intraocular pressure (IOP), ensuring visual quality, and guaranteeing the safety and efficacy of refractive surgeries [1-3]. Accurate assessment of corneal biomechanics is of great value for the early diagnosis of ocular diseases such as keratoconus and for postoperative mechanical risk evaluation.

Under normal physiological conditions, IOP subjects the cornea to an inflated stress state. Therefore, corneal inflation experiments have been widely used to investigate the biomechanical properties of the cornea under physiological IOP loading [4-7]. The related corneal inflation experimental problems can be broadly classified into two categories: one involves known initial corneal geometry, material properties, and boundary conditions of the inflation loading (such as fixation method and applied IOP), and requires solving for the corneal configuration under different boundary conditions. This category is referred to as the forward problem of corneal inflation experiments, i.e., forward prediction of the corneal inflated surface shape. The other category involves known initial corneal geometry, boundary conditions, and the corresponding inflated corneal configuration, and requires solving for the corneal constitutive parameters. This is known as the inverse problem of corneal inflation experiments, i.e., inversion of material parameters in the corneal constitutive model. The corneal surface information obtained from solving the forward problem is valuable for interpreting postoperative refractive surgery outcomes and vision changes in glaucoma patients; whereas the constitutive parameters identified through inverse analysis provide an important means to characterize the biomechanical properties of the cornea [8].

The finite element method (FEM), as a numerical solution technique, has been widely applied to both forward and inverse problems in corneal inflation experiments [9-11]. Bao et al. [12] employed FEM simulations to forward-predict the postoperative corneal surface shape and corresponding visual acuity under intraocular pressure in 28 patients who underwent LASIK refractive surgery. Their simulation results showed good agreement with clinical data. Zhou et al. [13] used FEM to predict the corneal surface deformation after PRK refractive surgery under IOP loading and evaluated the resulting regression in refractive power, providing guidance for the design of corneal ablation profiles. In inverse parameter identification, Zheng et al. [14] applied FEM-based inverse analysis on corneal inflation experiments to obtain the stress-strain relationship of rabbit corneas, facilitating studies related to physical intraocular pressure. Bao et al. [15] also conducted FEM inverse analysis on corneal inflation data from 20 diabetic and 20 normal rabbits to extract first-order Ogden constitutive model parameters, investigating the impact of diabetes on corneal biomechanical properties.

In addition to deterministic FEM-based inverse analysis, alternative strategies for inverse parameter identification have also been explored in recent years. Probabilistic and uncertainty-aware frameworks have been introduced to account for model uncertainty and measurement noise in inverse problems. For example, Soize [16] provided a comprehensive overview of uncertainty quantification and probabilistic learning on manifolds for multiscale inverse parameter identification in mechanics. These approaches emphasize the statistical characterization of material parameters and model uncertainties, offering a complementary perspective to deterministic inversion methods.

Nevertheless, despite the high accuracy and strong physical interpretability of FEM in forward modeling, it still faces significant challenges in solving inverse problems, particularly in tasks involving multi-parameter joint inversion and reconstruction of spatially distributed mechanical properties. First, traditional FEM relies on optimization algorithms to iteratively solve for model parameters. As the dimensionality of the parameters increases (e.g., simultaneous inversion of elastic modulus, Poisson's ratio, and heterogeneous distributions), the efficiency and stability of the solution rapidly decline, often leading to convergence to local minima or even inversion failure. Second, for complex biological tissues such as the cornea, which exhibit intricate geometry, material heterogeneity and nonlinear mechanics, traditional FEM struggles to support point-wise or regional inversion of mechanical parameters. As a result, it falls short in meeting the demands of high-resolution elasticity imaging, such as reconstructing three-dimensional maps of Young's modulus. Therefore, although FEM remains advantageous for forward simulations, new methodologies are urgently needed to address the limitations in full-field, multi-parameter inversion and personalized biomechanical modeling in the context of tissue heterogeneity.

Meanwhile, recent studies have proposed more sophisticated biomechanical models for corneal behavior. Dell'Isola et al. [17] developed a generalized plate model with kinematically independent thickness to describe corneal shapes affected by keratoconus before and after penetrating keratoplasty. Mazinani and Cardillo [18] combined shear wave velocity measurements with finite element modeling to investigate biomechanical differences between healthy and keratoconic corneas. These studies highlight ongoing efforts to improve physiological realism in corneal biomechanical modeling. While these models improve biomechanical fidelity, they typically rely on predefined constitutive assumptions and iterative inverse solvers.

In recent years, Physics-Informed Neural Networks (PINNs), an emerging technique that integrates physical laws with deep learning, have gained increasing attention. By embedding physical equations as soft constraints within the loss function of the neural network, PINNs enable models to maintain strong generalization performance even under limited data conditions. This approach has gradually been introduced into the inverse analysis of biomechanical parameters in soft biological tissues. Yin et al. [19] proposed a shear wave elastography network (SWENet) based on the PINN framework, in which the spatial variation of elastic properties in heterogeneous materials was incorporated into the governing equations and encoded in the loss function. The network was trained using wave field data at different time points, allowing the elastic properties within the region of interest (ROI) traversed by the shear wave to be simultaneously inferred. Kamali et al. [20] applied PINNs to the inverse elasticity problem, successfully reconstructing the spatial distributions of Young's modulus and Poisson's ratio by analyzing material strain response data under steady-state loading conditions, combined with external force measurements. This method demonstrated excellent performance not only in numerical simulations but also showed strong reliability when validated with experimental data. Ragoza et al. [21] proposed the use of PINNs to solve elastic inverse problems, offering a novel approach for magnetic resonance elastography (MRE). Their method does not rely on traditional numerical differentiation techniques but instead respects physical constraints while learning latent relationships from anatomical images. The study showed that, compared with conventional numerical methods, PINNs exhibited superior robustness to noise, produced better reconstruction results on real clinical data, and further improved the accuracy and reliability of elastography by integrating anatomical information. Zhang et al. [22] proposed a novel end-to-end deep learning model named Velocity Prediction Network (VP-Net), designed to accurately predict elastic wave velocity from raw optical coherence elastography (OCE) data of both healthy and abnormal human skin in vivo. Compared with traditional wave speed estimation methods, VP-Net achieved approximately a 100-fold increase in processing speed, and demonstrated highly accurate velocity predictions compared to other deep learning-based approaches, particularly due to its integration of physical information. Although several studies have successfully employed PINNs to invert material mechanical parameters from observational data, this approach has not yet been applied to corneal inflation experiments. Given that corneal inflation testing serves as an important method for evaluating corneal biomechanical properties, offering advantages such as ease of operation and well-defined mechanical responses, there is a pressing need to explore the application of PINN-based methods in this context to enable more efficient and fine-grained identification of corneal mechanical parameters.

In this study, a novel method based on the PINN framework is proposed for forward prediction and parameter inversion in the corneal inflation process, and its performance is compared with that of the traditional FEM. In the forward modeling of the corneal inflation experiment, given the initial geometry of the cornea, its material properties, and the boundary conditions of the inflation loading, the Physics-Informed Graph neural Galerkin Network (PIGGN) [23] was used to predict the corneal configuration under different IOP loads. In the inverse problem, given the initial geometry, the boundary conditions, and the deformed corneal configuration under corresponding loading, the constitutive material parameters of the cornea were identified. To validate the effectiveness of the proposed method, inflation experiments were conducted on artificial corneas made from Polydimethylsiloxane (PDMS) material, and the experimental results were compared with the model predictions. The results demonstrate that the proposed PINN-based method achieves high accuracy in both displacement prediction and material parameter inversion.

2. Materials and Methods

In this study, we adopted the PIGGN framework to model and analyze both the forward displacement prediction and inverse mechanical parameter identification of an artificial corneal phantom made of linearly elastic PDMS material under inflation testing. A comparative analysis was also conducted against FEM. This section provides a detailed description of the experimental setup, the principles and implementation of the PIGGN method, and the procedures of the finite element simulations.

2.1. Specimens and mechanical tests

This section provides a detailed description of the procedures involved in the artificial cornea inflation experiment, including: preparation of the artificial cornea phantom and artificial anterior chamber, compression testing for material property characterization, measurement and imaging systems, optical coherence tomography (OCT) image processing algorithm, and presentation of experimental results.

2.1.1. Preparation of artificial cornea phantom and artificial anterior chamber

PDMS and curing agent were mixed at a weight ratio of 10:1 to prepare a phantom material with mechanical properties similar to those of the native cornea [24]. The mixture was stirred thoroughly using a magnetic stirrer at 550 rpm for 30 minutes and then degassed in a vacuum chamber at -0.1 MPa for 15 minutes until the solution became clear. The degassed PDMS precursor was poured into a customized corneal mold and cured in a constant-temperature oven at 80 °C for 3 hours to obtain an artificial corneal phantom with standardized geometric features. As shown in Fig. 1A, the geometry of the corneal mold was designed based on the reference [25]. Figure 1B shows a photograph of the fabricated artificial cornea, while Fig. 1C illustrates the assembly of the artificial cornea with a light-cured 3D-printed chamber to form an artificial anterior chamber. By connecting the chamber to an external microfluidic pump and pressure sensor through tubing, the internal pressure can be precisely regulated.

2.1.2. Compression testing to obtain mechanical parameters of materials

To determine the Young's modulus of the PDMS material, an universal testing machine (TH-8203S, Tophung, China) was used to perform compression tests on cylindrical PDMS specimens with a diameter of 20 mm and a height of 40 mm. The specimens were subjected to uniaxial compression at a constant speed of 20 mm/min, and the loading-unloading cycle was repeated six times to minimize experimental error. The light blue shaded region in Fig. 2B represents the stress–strain data obtained from the six compression tests. Given that the change in central corneal thickness during the subsequent inflation experiments remains within 5% of the initial thickness, only the linear region corresponding to a strain range of 0–0.05 was used for curve fitting. The resulting Young's modulus of the PDMS material was approximately 1312.6 kPa, which was later considered the ground-truth Young's modulus in subsequent evaluations. The cornea exhibits nearly incompressible behavior under mechanical loading. In accordance with prior biomechanical studies [26-29], a Poisson's ratio of 0.49 was adopted for the corneal tissue in this analysis.

2.1.3. Measurement and imaging systems

The inflation experiment setup for the artificial cornea, as shown in Fig. 3, consists of two main components: the IOP control system and the image acquisition system.

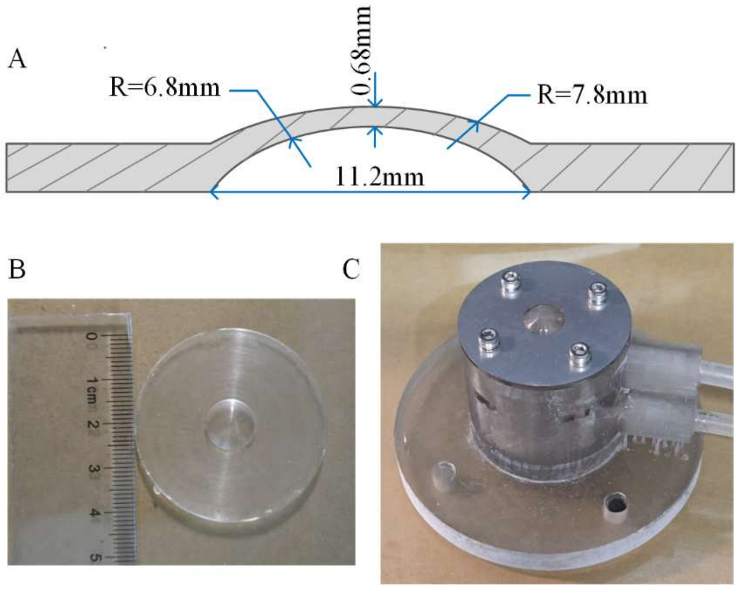

Fig. 1. Photographs of the artificial cornea and artificial anterior chamber, (A) Cross-sectional view of the artificial cornea geometry, showing a central thickness of 0.68 mm, a base width of 11.2 mm, and anterior/posterior curvature radii of 7.8 mm and 6.8 mm, respectively, featuring a thinner center and thicker periphery, (B) Photograph of the fabricated artificial cornea, (C) Photograph of the assembled artificial anterior chamber.

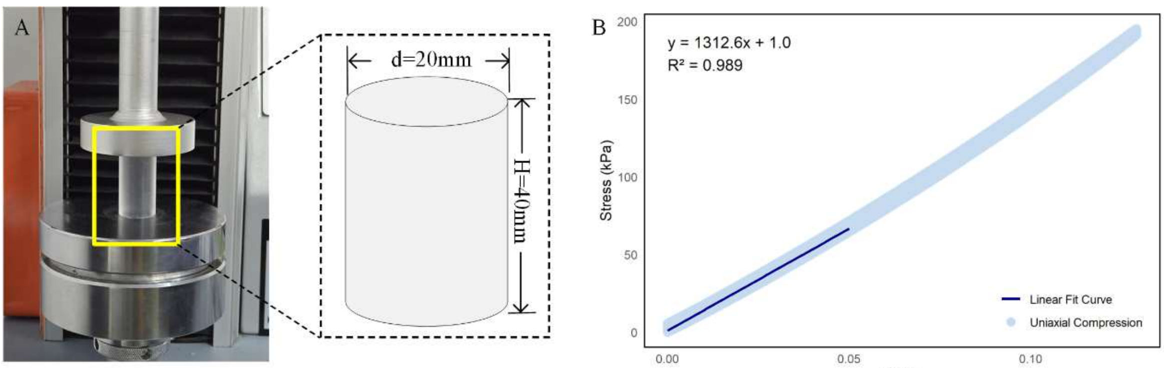

Fig. 2. Geometry of the compression phantom and experimental results, (A) Schematic of the compression setup and the geometry of the phantom, (B) Compression test results. The light blue shaded area represents stress–strain data from six repeated tests, indicating a linear relationship between stress and strain. A linear fit in the strain range of 0–0.05 yields a Young's modulus of approximately 1312.6 kPa.

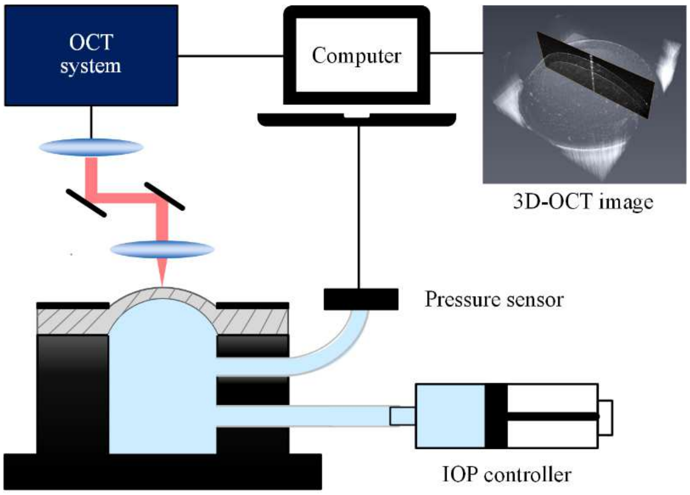

Fig. 3. Schematic of the corneal inflation experiment setup. The system consists of an intraocular pressure control module and an image acquisition module.

In the IOP control system, a microfluidic pump and a pressure sensor are connected to the artificial anterior chamber. The microfluidic pump regulates the IOP, while the pressure sensor, placed at the same height as the corneal apex, is connected in series to a physiological recorder (PowerLab T26-8478, ADInstruments, Australia). This setup enables real-time digital acquisition of IOP signals at a sampling frequency of 100 kHz.

For image acquisition, a spectral-domain optical coherence tomography (SD-OCT) system [11] is used to capture three-dimensional structural images of the cornea. A broadband light source (SLD850S-A10W, Thorlabs, USA) emits a beam that is split into two paths by a 50:50 fiber coupler (TW850R5A2, Thorlabs, USA), directing light to both the sample arm and the reference arm. In the sample arm, the collimated beam is directed onto a scanning galvanometer (UltraScan-II-7mm, Han's Laser, China), and then focused onto the sample by a lens (AC254-050-B, Thorlabs, USA). In the reference arm, the beam is also collimated and passed through an identical lens, then reflected back by a mirror assembly. The returning beams from both arms are recombined at the fiber coupler, producing interference which is then sent to the spectrometer. The spectrometer consists of a collimating lens (F280APC-850, Thorlabs, USA), a diffraction grating (GR13-0608, Thorlabs, USA), a focusing lens (AC254-040-B, Thorlabs, USA), and a line-scan camera (LA-GM-02K08A, Teledyne DALSA, China). Data acquisition and scan control of the SD-OCT system are handled by a data acquisition card (PCIE9311N, Altech, China).

Using the pressure control system, the IOP was increased stepwise from 0 mmHg to 100 mmHg in 20 mmHg increments. Before each measurement, the pressure was allowed to stabilize. An SD-OCT system was used to acquire three-dimensional structural images of the cornea under different pressure loads. To minimize experimental errors, the loading–unloading process was repeated six times, yielding six sets of 3D-OCT images of the same corneal sample under varying IOP conditions.

2.1.4. OCT image processing

Given the axisymmetric geometry of the artificial cornea, signal extraction and analysis were performed only on the longitudinal cross-section passing through the corneal apex. As shown in Fig. 4, to accurately extract the anterior surface profile of the cornea from OCT images, a contour extraction algorithm based on intensity extremum detection and Random Sample Consensus (RANSAC) ellipse fitting was developed. The algorithm consists of three main steps: point extraction, ellipse fitting, and contour reconstruction.
Input: Grayscale OCT image.

Step 1: Point Extraction

For each column x in the image, the pixel with the maximum grayscale value is identified, assuming it corresponds to the high-reflectivity signal of the anterior corneal surface. Each (x,y) coordinate is recorded as a candidate point, forming the initial set of contour points.

Step 2: RANSAC Ellipse Fitting

To improve robustness against noise and interference from the posterior surface, the RANSAC is used for ellipse fitting. In each iteration, five points are randomly selected to estimate ellipse parameters, and the number of inliers (points close to the fitted ellipse) is calculated. The ellipse with the highest inlier count is retained as the optimal fit. If any posterior surface points are detected in the result, they are removed and the fitting process is repeated.

Step 3: Contour Generation

Based on the finalized set of anterior surface points, linear interpolation is applied to fill in missing regions, generating a continuous contour curve. The output is a set of (x,y) coordinate pairs.
Output: A set of (x,y) coordinates representing the profile of the anterior corneal surface.

Figure 4A illustrates the application of the proposed algorithm for anterior corneal surface contour extraction. The axial resolution of the OCT image was experimentally calibrated to be 3.96 μm, As shown in Fig. 4A, the extracted contour points closely match the actual high-reflectivity boundary in the image, demonstrating the high accuracy of the method. Figure 4B provides an overview of the entire contour extraction pipeline, including point extraction, RANSAC-based ellipse fitting, and contour reconstruction.

To compute the anterior surface displacement under different intraocular pressures, the extracted contour points at each IOP level were subtracted from those at 0 mmHg. Due to strong noise at the image edges, only the region within a 4 mm radius around the corneal apex was used for contour analysis.

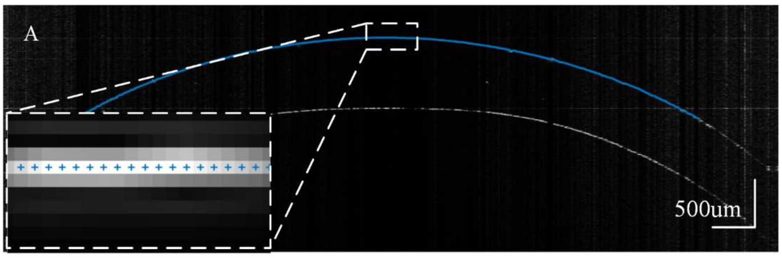

B

Algorithm for extracting contour points on the anterior surface of cornea

Input: Gray image

Steps:

1.Extract Points:

For each column x, find y with max intensity → store (x, y).

2.Fit Ellipse (RANSAC):

Repeat N times:

Pick 5 random points → fit ellipse.

Keep ellipse with most inliers (points close to curve).

if posterior_detected: remove_points(); repeat 2.

3.Generate Contour:

For all x, compute y from linear interpolation → output (x, y) pairs.

Output: (x, y) paris

Fig. 4. Algorithm for extracting anterior surface signal points from 2D cross-sectional OCT images of the artificial cornea, (A) Demonstration of the extracted anterior surface signal points from an OCT cross-sectional image in a representative experiment. The zoomed-in view shows that the extracted points closely match the actual high-reflectivity boundary, indicating high accuracy of the proposed method, (B) Pseudocode of the anterior surface signal point extraction algorithm.

2.2. PIGGN modeling and solving methods

This study introduces the adopted PIGGN model [23] to perform both forward and inverse modeling of the corneal inflation process. Specifically, in the forward prediction task, the model takes as input the known mechanical properties of the material, the geometric mesh, and boundary loading conditions to predict the corneal displacement response under a given IOP. In the inverse identification task, the model uses the geometric structure, boundary conditions, and the experimentally measured displacement field on the corneal surface to infer the underlying mechanical parameters of the material. This section provides a brief overview of the principles behind the forward and inverse solutions using PIGGN.

PIGGN is a method based on the concept of PINNs designed to solve PDEs within specific physical domains. Similar to traditional FEM, PIGGN requires mesh discretization of the solution domain. However, unlike FEM which assembles a stiffness matrix based on the principle of minimum potential energy and solves for nodal solutions, PIGGN transforms the mesh into a graph structure and employs Graph Convolutional Networks (GCNs) to perform convolution operations and feature extraction on the graph. The GCN then directly outputs the solution at each mesh node.

In terms of loss function construction, PIGGN transforms the PDEs into their weak form based on the Galerkin variational principle. The continuous integrals are then approximated using Gaussian quadrature, which expresses them as weighted sums over specific integration points. This loss function incorporates the governing physical equations into the network training process and is employed during backpropagation to optimize the parameters of the GCN.

After obtaining the nodal solutions, PIGGN employs shape functions to interpolate the physical fields, yielding a continuous full-field solution. This approach not only inherits the advantage of PINNs in incorporating physical laws into neural network training but also leverages the capability of GCN in handling unstructured meshes, enabling efficient modeling and solution of complex physical fields.

2.2.1. *Forward prediction*

We first discretize the physical domain using quadratic 27-node hexahedral elements, in which the field variables within each element are interpolated using second-order Lagrange polynomials. In this study, we employ a total of 358 elements and 3,785 nodes, as shown in Fig. 5A. The resulting unstructured mesh, composed of nodes and edges, can be naturally represented as a graph (Fig. 5B). In this graph representation, each node is characterized by its spatial coordinates (x,y,z), and its connections to other nodes are defined by an adjacency matrix. To preserve physical locality and ensure computational efficiency, the adjacency matrix strictly encodes connections only to immediate neighboring nodes based on the local mesh topology.

In practical physical problems, boundaries are often irregular in shape. Unstructured meshes based on graph representations offer superior adaptability to complex boundaries, making them well-suited for modeling intricate geometries. GCN can perform convolution operations and feature extraction directly on such graph structures. To predict different physical quantities, we construct separate subnetworks for each displacement component, corresponding to the prediction of displacements in the x, y, and z directions, respectively.

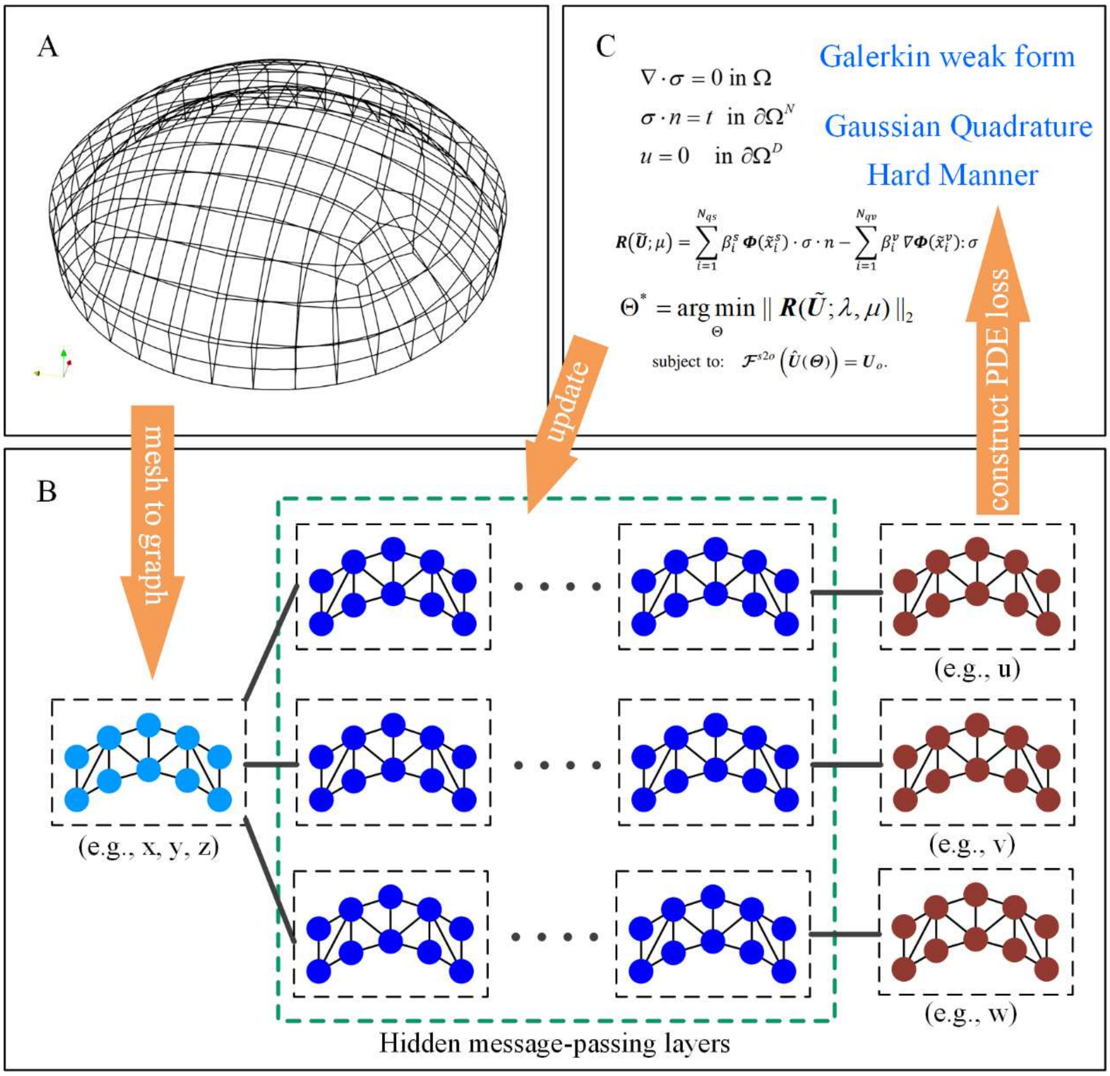

Fig. 5. Workflow of PIGGN modeling for forward and inverse corneal inflation problems, (A) The physical domain is discretized using second-order nonlinear 27-node hexahedral elements. In this study, 358 elements and a total of 3785 nodes are used. The resulting unstructured mesh, consisting of nodes and edges, can be naturally represented as a graph, (B) GCN architecture. Graph convolution is performed on the unstructured mesh. Each physical variable is modeled by a separate subnet. The input includes the spatial coordinates (x, y, z) of the nodes and their connectivity, and the outputs of the three subnets correspond to displacements in the x, y, and z directions, respectively, (C) The Galerkin method is used to convert the PDEs into their weak form, and Gaussian quadrature is applied to compute the integrals over element volumes and surfaces. Dirichlet boundary conditions are enforced via hard constraints. The resulting physics-informed loss is used to update the parameters of the GCN.

This study employs the Chebyshev graph convolution operator [26] for graph convolution operations, with the convolution kernel order K set to 10 to enhance the model's capacity to capture local structures. The layer architecture of each subnetwork is configured as [3, 32, 64, 128, 256, 128, 64, 32, 1], where 3 denotes the input dimension per node (i.e., spatial coordinates), and the output corresponds to the displacement prediction in the respective direction for each node. All hidden layers utilize the ReLU activation function to improve the network's nonlinear representation ability.

Subsequently, the physical information loss is constructed based on the grid solution output by the GCN. Let $\widetilde{\boldsymbol{U}}$ denote the nodal solution output by the GCN, and $\boldsymbol{\Phi}(x)$ represent the vector of second-order Lagrange basis functions. By performing basis function interpolation on the nodal solution, we obtain the approximate full-field solution, i.e.,

$$\widetilde{\boldsymbol{u}}_{\boldsymbol{h}}(x;\widetilde{\boldsymbol{U}})=\boldsymbol{\Phi}(x)^T\widetilde{\boldsymbol{U}} \tag{1}$$

Here $\widetilde{\boldsymbol{u}}_{\boldsymbol{h}}=[u_x,u_y,u_z]$, and the subscript h refers to the discretized solution in a finite-dimensional Hilbert subspace spanned by the chosen basis functions. Next, we calculate the physics-informed loss. The linear elasticity equations can be written as:

$$\begin{aligned}\nabla\cdot\boldsymbol{\sigma} &=0 && \text{in } \Omega\\ \boldsymbol{\sigma}\cdot\boldsymbol{n} &=\boldsymbol{t} && \text{on } \partial\Omega^N\\ \boldsymbol{u} &=0 && \text{on } \partial\Omega^D\end{aligned} \tag{2}$$

Here, the effect of body forces is neglected, as their influence on the results is minimal [27]. $\boldsymbol{\sigma}$ denotes the Cauchy stress tensor, Ω denotes the physical domain to be solved. $\partial\Omega^N$ represents the Neumann boundary, where external forces $\boldsymbol{t}$ are applied — in our case, this corresponds to the intraocular pressure acting on the posterior surface of the cornea. $\partial\Omega^D$ denotes the Dirichlet boundary, where the displacement is fixed to zero. In our inflation experiment, this corresponds to the lateral boundary of the cornea.

The stress–strain relationship of isotropic linear elastic material is described by the constitutive equation in index notation:

$$\sigma_{ij} = \lambda \delta_{ij} \varepsilon_{kk} + 2\mu \varepsilon_{ij} \tag{3}$$

where λ and μ are the Lamé constants, δ_{ij} is the Kronecker delta, and the strain tensor is defined as:

$$\varepsilon_{ij} = \frac{1}{2}\left(\frac{\partial u_i}{\partial x_j} + \frac{\partial u_j}{\partial x_i}\right) \tag{4}$$

The governing equations (2) are transformed from their original differential form into a weak integral form via the Galerkin method. Applying the divergence theorem, the integral form of the governing equations is reformulated. Finally, Gaussian quadrature is employed to convert the continuous integrals into a weighted sum of basis functions evaluated at discrete points, the details are as follows:

To formulate the continuous Galerkin method, we first define the standard Sobolev space $[\mathcal{H}^1(\Omega)]^3$ for the three-dimensional displacement field, where weak derivatives up to order one is square-integrable. We construct the finite element trial space $\mathcal{V}_h^p$ using continuous piecewise polynomial basis functions over the hexahedral mesh $\mathcal{E}_h$:

$$\mathcal{V}_h^p = \{\mathbf{v} \in [\mathcal{H}^1(\Omega)]^3 \mid \mathbf{v}|_K \in [\mathcal{P}_p(K)]^3, \forall K \in \mathcal{E}_h\} \tag{5}$$

where $\mathcal{P}_p(K)$ is the space of polynomial functions of degree up to p defined on the element K.

We introduce a test function $\boldsymbol{\omega}_h \in \mathcal{V}_h^p$. To satisfy kinematic admissibility, the test function must vanish on the Dirichlet boundary. Thus, the test space is specifically defined as:

$$\mathcal{V}_{h,0}^p = \{\boldsymbol{\omega}_h \in \mathcal{V}_h^p \mid \boldsymbol{\omega}_h = \mathbf{0} \text{ on } \partial\Omega^D\} \tag{6}$$

We multiply the strong form of the equilibrium equation by the arbitrary test function $\boldsymbol{\omega}_h \in \mathcal{V}_{h,0}^p$ and integrate over the entire domain Ω:

$$\int_\Omega (\nabla \cdot \boldsymbol{\sigma}) \cdot \boldsymbol{\omega}_h dV = 0 \tag{7}$$

Applying the divergence theorem (integration by parts) yields the equivalent weak formulation of the PDEs:

$$\int_\Omega \nabla \boldsymbol{\omega}_h : \boldsymbol{\sigma}(\mathbf{u}_h) dV - \int_{\partial\Omega^N} \boldsymbol{\omega}_h \cdot \mathbf{t} dS = 0 \tag{8}$$

where $\mathbf{u}_h \in \mathcal{V}_h^p$ is the trial solution satisfying $\mathbf{u}_h = \mathbf{u}^D$ on $\partial\Omega^D$. Note that the body force is omitted here, matching the strong form.

In this work, the trial space $\mathcal{V}_h^p$ is constructed using second-order continuous piecewise polynomial basis functions defined on a 27-node hexahedral element mesh. We introduce a basis shape function matrix $\mathbf{\Phi}(\mathbf{x}) \in \mathbb{R}^{N_U \times N_c}$ to express the test variables as $\boldsymbol{\omega}_h(\mathbf{x}) = \mathbf{\Phi}(\mathbf{x})^T \widetilde{\boldsymbol{W}}$, where $\widetilde{\boldsymbol{W}}$ represents the arbitrary coefficients (virtual nodal displacements) of the test variable. The trial function is similarly approximated as $\mathbf{u}_h(\mathbf{x}) = \mathbf{\Phi}(\mathbf{x})^T \widetilde{\boldsymbol{U}}$. Substituting these into the weak form leads to the discrete Galerkin equivalent:

$$\widetilde{\boldsymbol{W}}^T \left[\int_\Omega \nabla \mathbf{\Phi} : \boldsymbol{\sigma}(\mathbf{u}_h; \widetilde{\boldsymbol{U}}) dV - \int_{\partial\Omega^N} \mathbf{\Phi} \cdot \mathbf{t} dS \right] = 0 \tag{9}$$

For a specific type of element, the coordinates of the Gaussian quadrature points on the volume $\tilde{x}_i^s (i = 1,2,\dots,N_{qs})$ and surface $\tilde{x}_i^v (i = 1,2,\dots,N_{qv})$, as well as the corresponding integration weights $\beta_i^s (i = 1,2,\dots,N_{qs})$ and $\beta_i^v (i = 1,2,\dots,N_{qv})$, can be precomputed.Based on the above procedure, the discrete PDE residual $\mathbf{R}(\widetilde{\boldsymbol{U}}; \lambda, \mu)$ to be minimized during network training is formulated as:

$$\begin{aligned} \boldsymbol{R}\big(\widetilde{\boldsymbol{U}}; \lambda, \mu\big) &= \sum_{i=1}^{N_{qs}} \beta_i^s \boldsymbol{\Phi}(\tilde{x}_i^s) \cdot \sigma \bullet n - \sum_{i=1}^{N_{qv}} \beta_i^v \nabla \boldsymbol{\Phi}(\tilde{x}_i^v) : \sigma \\ &= \sum_{i=1}^{N_{qs}} \beta_i^s \boldsymbol{\Phi}(\tilde{x}_i^s) \cdot t - \sum_{i=1}^{N_{qv}} \beta_i^v \nabla \boldsymbol{\Phi}(\tilde{x}_i^v) : \big(\mu \nabla^2 \widetilde{\boldsymbol{u}}_{\boldsymbol{h}} + (\lambda + \mu) \nabla (\nabla \cdot \widetilde{\boldsymbol{u}}_{\boldsymbol{h}})\big) \end{aligned} \tag{10}$$

Here ∇^2 denotes the Laplacian operator, $\nabla^2 \widetilde{\boldsymbol{u}}_{\boldsymbol{h}} = [\nabla^2 u_x, \nabla^2 u_y, \nabla^2 u_z]$, $\nabla(\nabla \cdot \widetilde{\boldsymbol{u}}_{\boldsymbol{h}})$ is the gradient of the divergence of the displacement field, $\nabla(\nabla \cdot \widetilde{\boldsymbol{u}}_{\boldsymbol{h}}) = [\frac{\partial}{\partial x}(\nabla \cdot \widetilde{\boldsymbol{u}}_{\boldsymbol{h}}), \frac{\partial}{\partial y}(\nabla \cdot \widetilde{\boldsymbol{u}}_{\boldsymbol{h}}), \frac{\partial}{\partial z}(\nabla \cdot \widetilde{\boldsymbol{u}}_{\boldsymbol{h}})]$, $\nabla \cdot \widetilde{\boldsymbol{u}}_{\boldsymbol{h}}$ is the divergence of the displacement field, $\nabla \cdot \widetilde{\boldsymbol{u}}_{\boldsymbol{h}} = \frac{\partial u_x}{\partial x} + \frac{\partial u_y}{\partial y} + \frac{\partial u_z}{\partial z}$. The expression$\mu \nabla^2 \widetilde{\boldsymbol{u}}_{\boldsymbol{h}} + (\lambda + \mu) \nabla(\nabla \cdot \widetilde{\boldsymbol{u}}_{\boldsymbol{h}})$ corresponds to the Navier–Lamé equations, which can be written in matrix form as:

$$\mu \begin{bmatrix} \dfrac{\partial^2 u_x}{\partial x^2} + \dfrac{\partial^2 u_x}{\partial y^2} + \dfrac{\partial^2 u_x}{\partial z^2} \\ \dfrac{\partial^2 u_y}{\partial x^2} + \dfrac{\partial^2 u_y}{\partial y^2} + \dfrac{\partial^2 u_y}{\partial z^2} \\ \dfrac{\partial^2 u_z}{\partial x^2} + \dfrac{\partial^2 u_z}{\partial y^2} + \dfrac{\partial^2 u_z}{\partial z^2} \end{bmatrix} + (\lambda + \mu) \begin{bmatrix} \dfrac{\partial}{\partial x}\left(\dfrac{\partial u_x}{\partial x} + \dfrac{\partial u_y}{\partial y} + \dfrac{\partial u_z}{\partial z}\right) \\ \dfrac{\partial}{\partial y}\left(\dfrac{\partial u_x}{\partial x} + \dfrac{\partial u_y}{\partial y} + \dfrac{\partial u_z}{\partial z}\right) \\ \dfrac{\partial}{\partial z}\left(\dfrac{\partial u_x}{\partial x} + \dfrac{\partial u_y}{\partial y} + \dfrac{\partial u_z}{\partial z}\right) \end{bmatrix} \tag{11}$$

The Neumann boundary condition is naturally embedded into the loss function. For the Dirichlet boundary condition, we adopt a hard data assimilation strategy [23] inspired by the concept of static condensation. Instead of adding a penalty term, the constraints are satisfied automatically by construction.

Algorithmically, the full-field degrees of freedom (DOFs) predicted by the GCN, denoted as $\widetilde{\mathbf{U}}(\Theta)$, are partitioned into unconstrained DOFs, $\widetilde{\mathbf{U}}_u(\Theta)$, and constrained DOFs corresponding to the observation points. To strictly impose the Dirichlet boundary conditions, we construct an assembled displacement field $\widehat{\mathbf{U}}$ by retaining the network predictions for the unconstrained regions, while directly replacing the constrained DOFs with the experimentally measured boundary values $\mathbf{U}_o$. Mathematically, the assembled field is defined as $\widehat{\mathbf{U}} = [\widetilde{\mathbf{U}}_u(\Theta)^T, \mathbf{U}_o^T]^T$.

After constructing this full-field displacement dataset that exactly satisfies the hard Dirichlet boundary conditions, the physics-informed residual $\mathbf{R}$ is subsequently computed. Consequently, the original constrained optimization problem is effectively recast as an unconstrained minimization problem over the network parameters Θ:

$$\Theta^* = \arg\ \min_{\Theta} \| \mathbf{R}(\widehat{\mathbf{U}}(\widetilde{\mathbf{U}}_u(\Theta), \mathbf{U}_o); \lambda, \mu) \|_2 \tag{12}$$

In this formulation, the state-to-observable constraints are strictly preserved before backpropagation, circumventing the optimization challenges associated with competing loss terms in conventional soft-constrained PINNs.

2.2.2. Inverse parameter identification

For the inverse parameter identification problem, the observed displacements on the anterior surface of the cornea are incorporated into the Dirichlet boundary condition, and the mechanical parameters λ and μ are treated as trainable variables. The problem is then reformulated as:

$$(\Theta^*, \lambda^*, \mu^*) = \arg\min_{\Theta,\lambda,\mu} \| \boldsymbol{R}(\widetilde{\boldsymbol{U}}; \lambda, \mu) \|_2 \ \text{ subject to: } F^{s2o}(\widetilde{\boldsymbol{U}}(\Theta; \lambda, \mu)) = U_o \tag{13}$$

2.3. FE modeling and solving methods

The FEM is a conventional approach commonly used for forward modeling of corneal inflation experiments and inverse estimation of mechanical parameters. To provide a comparison with the proposed PIGGN framework, this section presents the FEM-based methodology.

2.3.1. Forward prediction

The finite element modeling was implemented using the commercial software COMSOL Multiphysics 6.2. The modeling process followed the standard finite element analysis (FEA) workflow, including geometry construction, assignment of material properties, application of boundary conditions, mesh generation, and solver configuration.

Figure 6A illustrates the geometry and boundary condition settings. The model dimensions are consistent with those of a real cornea, with a radius of curvature of $R_2 = 7.8\text{mm}$ for the anterior surface, $R_1 = 6.8\text{mm}$ for the posterior surface, and a central thickness of $T = 680\mu\text{m}$. The peripheral boundary of the cornea is fixed, and a uniform intraocular pressure P is applied to the posterior surface. The corneal tissue is modeled as a nearly incompressible linear elastic material, with a Young's modulus of 1312.6 kPa and a Poisson's ratio of 0.49. Figure 6B shows the full 3D geometry of the cornea along with the corresponding finite element mesh. The displacement response under pressure loading is obtained using the steady-state solver module in COMSOL.

2.3.2. Inverse parameter identification

In the absence of a known Young's modulus, the optimal value can be obtained by iteratively updating the parameter E to minimize the residual between the predicted and experimentally measured apex displacement. This leads to a least-squares optimization problem formulated as:

$$\min_{E}(\phi), \phi = \frac{1}{2}\sum_{i}^{N}(y_i(E) - y_i^e)^2 \tag{14}$$

Here, y_i^e denotes the observed apex displacement. In our experiment, the total number of data samples is $N = 5$ corresponding to apex displacements under intraocular pressure increments of 20 mmHg, 40 mmHg, 60 mmHg, 80 mmHg, and 100 mmHg relative to 0 mmHg. E represents the Young's modulus to be iteratively optimized, and denotes the apex displacement computed using the finite element method with the given Young's modulus E. The Levenberg-Marquardt algorithm is then employed to iteratively update the model parameters until the loss function falls below the specified tolerance of 0.001.

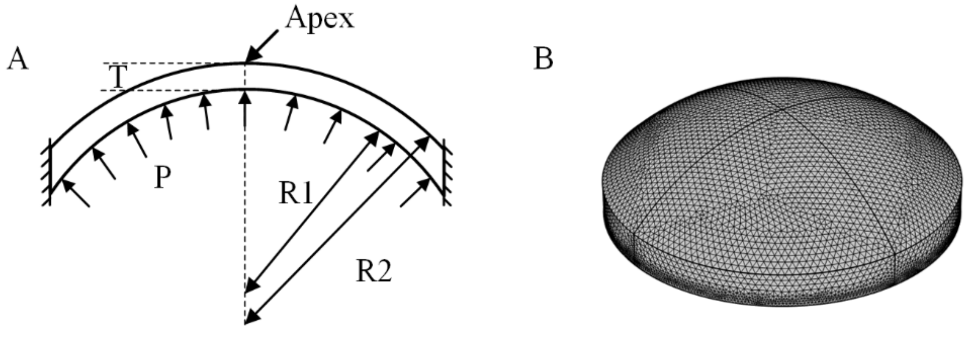

Fig. 6. Schematic of the corneal mechanical model and finite element mesh, (A) Geometry and boundary condition setup. The radius of curvature is $R_2 = 7.8\text{mm}$ for the anterior surface and $R_1 = 6.8\text{mm}$ for the posterior surface. The central corneal thickness is $T = 680\mu\text{m}$. The peripheral boundary is fixed, and a uniform intraocular pressure P is applied to the posterior surface, (B) Finite element mesh diagram.

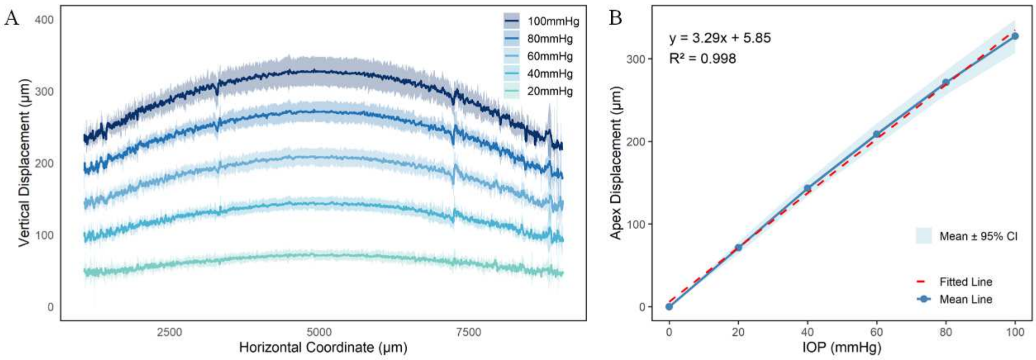

Fig. 7. Results of the artificial cornea inflation experiment, (A) Anterior surface displacement of the artificial cornea within a central region of 4 mm radius under varying intraocular pressure (IOP), (B) Apical displacement of the anterior surface as a function of IOP. For each IOP level, six repeated measurements were performed; blue dots represent the mean values, light blue shading indicates the 95% confidence interval, and the red dashed line denotes the linear regression fit. The experimental data show that an increase of 1 mmHg in IOP results in approximately 3.29 μm of apical displacement.

3. Results

This section presents the results of forward displacement prediction and inverse parameter identification in the corneal inflation experiment, using the PIGGN network described in Section 2.2 and the FE Method introduced in Section 2.3. These results are compared against the experimental measurements reported in Section 2.1.

3.1. Experimental results

Figure 7 illustrates the experimental measurements of the anterior surface displacement of the artificial cornea under varying IOP conditions. As shown in Fig. 7A, within a central region of 4 mm in radius, the displacement of the anterior corneal surface increases progressively with rising IOP, while maintaining a high degree of symmetry across all pressure levels. Solid lines represent the mean of 6 repeated measurements at each pressure level, and the shaded areas indicate the corresponding 95% confidence intervals, reflecting the high reproducibility and reliability of the measurements.

Figure 7B quantitatively characterizes the relationship between corneal apical displacement and IOP. Blue markers indicate the mean values from six repeated measurements, the light blue shaded region represents the 95% confidence interval, and the red dashed line corresponds to the linear regression fit. The fitted equation is y = 3.29x + 5.85, with a coefficient of determination R^2 = 0.998, indicating a strong linear correlation between apical displacement and IOP. The slope of 3.29 suggests that apical displacement increases by approximately 3.29 μm for each 1 mmHg rise in IOP, demonstrating that the artificial cornea exhibits well-defined linear elastic behavior within the tested pressure range.

3.2. PIGGN results

Figure 8 illustrates the predicted displacement fields under various IOP conditions during the corneal inflation experiment using the PIGGN network, along with comparisons to experimental measurements. Figures 8A to 8F correspond to the predicted full-field axial (Z-direction) displacement distributions of the cornea under IOPs of 0, 20, 40, 60, 80, and 100 mmHg, respectively. The results indicate that corneal displacement increases linearly with rising IOP and is predominantly concentrated in the central region. The closer to the corneal apex, the more pronounced the deformation becomes.

Figure 8G compares the experimentally measured displacement profile of the anterior corneal surface with the prediction from the PIGGN network. The solid line represents the experimental data, while the dashed line denotes the network simulation. The results show good agreement in the central region of the cornea, whereas noticeable deviations are observed near the periphery.

Figure 8H provides a quantitative analysis of the relationship between apex displacement of the anterior corneal surface and intraocular pressure (IOP). The PIGGN-predicted apex displacement exhibits a clear linear trend with increasing IOP, with a fitted slope of 3.41 μm/mmHg and R^2 = 1.000. Compared to the experimentally derived linear fit (3.29 μm/mmHg; see Fig. 7B), the relative error is 3.6%, demonstrating the high accuracy of the model in predicting apex displacement.

After completing the forward modeling, Fig. 8I–J illustrate the performance of the PIGGN network in solving the inverse problem of the corneal inflation experiment—specifically, the reconstruction of mechanical parameters λ and μ given the known corneal geometry, boundary conditions, and steady-state displacement field. As shown in Fig. 8I, the model converges after approximately 1200 training epochs, with λ stabilizing at approximately 21,625,949.1 and μ at 441,345.9. These values correspond to a Young's modulus of 1315.2 kPa, which is very close to the experimentally measured modulus of 1312.6 kPa from compression testing, with a relative error of only 0.2%. The inferred Poisson's ratio is 0.49, demonstrating high consistency with the experimental value. Figure 8J presents the convergence trend of the loss function during the inversion process, further confirming the stability and effectiveness of the optimization procedure.

To ensure the exact reproducibility of the proposed model, the detailed training hyperparameters are explicitly specified. The graph neural network architecture consists of 7 hidden layers and employs the ReLU activation function to capture non-linearities. The model was trained for a total of 1200 epochs with a batch size of 1. We utilized the Adam optimizer [30] with a constant learning rate of 1e-3. All computational procedures, including network training and physics-informed loss evaluation, were executed on an NVIDIA GeForce RTX 4090 GPU.

3.3. FEM Results

The finite element method is a widely used numerical approach for solving both forward and inverse problems in corneal inflation experiments. Figure 9 demonstrates the FEM-based predictions of corneal mechanical behavior in forward analysis and parameter identification in inverse analysis. Figures 9A to 9F display the Z-axis displacement contours on the anterior corneal surface under progressively increasing IOP levels of 0, 20, 40, 60, 80, and 100 mmHg, respectively. The results reveal that corneal displacement exhibits a graded increase with elevating IOP, with maximum displacement concentrated in the central region, demonstrating characteristic axisymmetric deformation patterns.

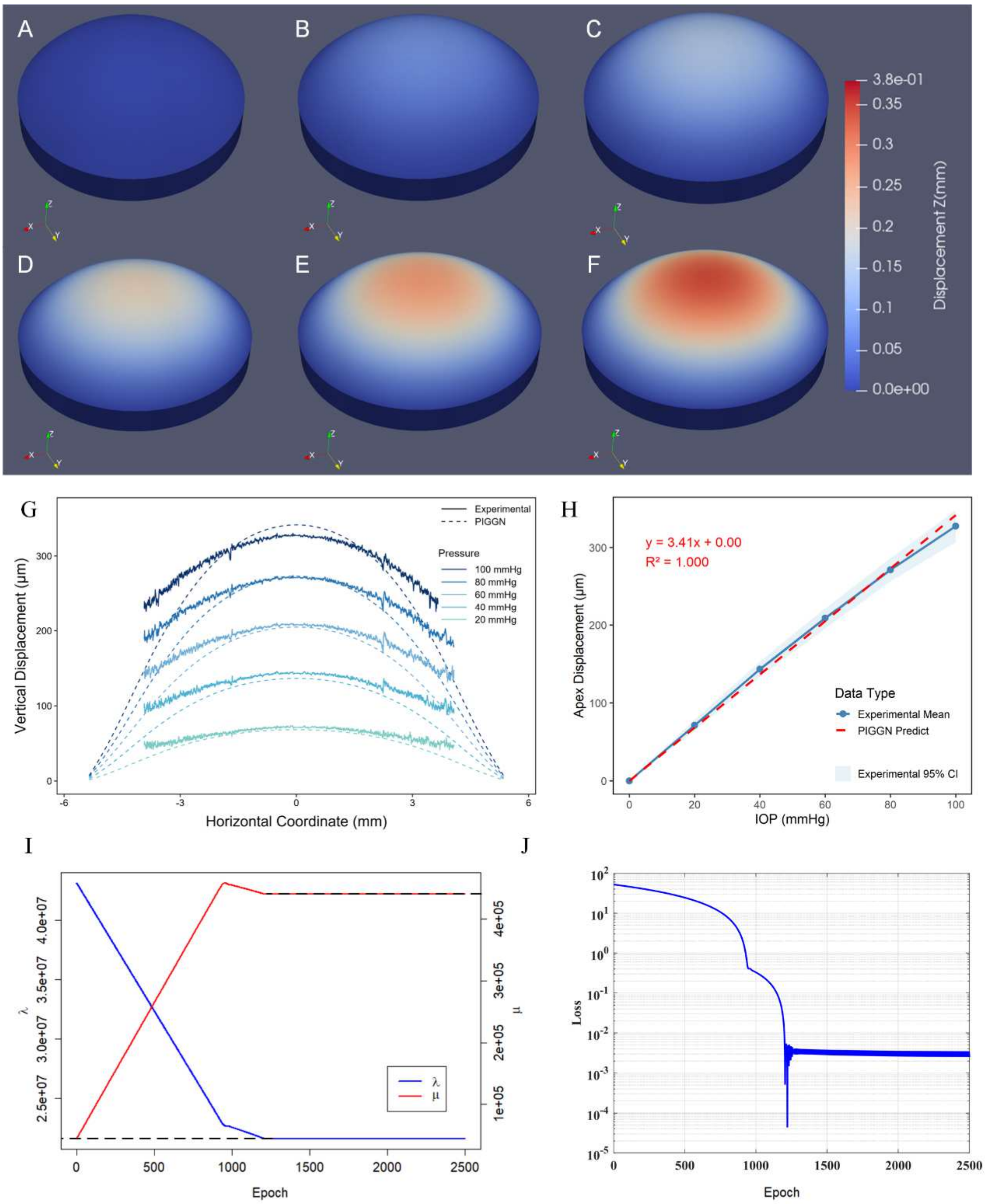

Fig. 8. Prediction and Inverse Parameter Identification of Corneal Inflation Experiment Based on the PIGGN Network, (A–F) Predicted full-field axial (Z-direction) displacement of the cornea under different IOP, corresponding to 0, 20, 40, 60, 80, and 100 mmHg, respectively. Displacement is primarily concentrated in the central region of the cornea and increases linearly with IOP, (G) Comparison between the PIGGN-predicted Z-direction displacement on the corneal anterior surface and the experimentally measured data. The solid line represents the mean of experimental results, while the dashed line denotes the predicted values, (H) Comparison of the PIGGN-predicted apex axial displacement with experimental measurements. The red dashed line indicates the predicted results, showing a linear trend with IOP, with a fitted slope of 3.41 μm/mmHg. The blue solid line and shaded region represent the experimental mean and its 95% confidence interval (3.29 μm/mmHg; see Fig. 7B), yielding a relative error of 3.6%, (I) Evolution of the Lamé parameters (λ and μ) during the training process under the known displacement field. Convergence is achieved after approximately 1200 training epochs, with λ stabilizing at ~21,625,949.1 and μ at ~441,345.9. The corresponding Young's modulus is 1315.2 kPa, closely matching the compression test result of 1312.6 kPa, with a relative error of 0.2%. The inferred Poisson's ratio converges to 0.49, showing high consistency with the experimental value. (J) Evolution of the loss function during the inversion process.

Figure 9G compares the FEM-predicted results with experimentally measured axial displacement curves of the anterior corneal surface. The solid line represents experimental data, while the dashed line indicates FEM simulation results. The results show good agreement in the central region, with minor deviations observed in the peripheral zone.

Figure 9H compares the FEM-predicted trend of corneal apex displacement with IOP variation against experimental mean values. The results demonstrate excellent agreement between FEM predictions and experimental data: The linear regression slope was 3.37 μm/mmHg for FEM simulations, showing merely a 2.4% relative error compared with the experimental fitting result (3.29 μm/mmHg, Fig. 7B), which confirms the high predictive accuracy of the finite element model.

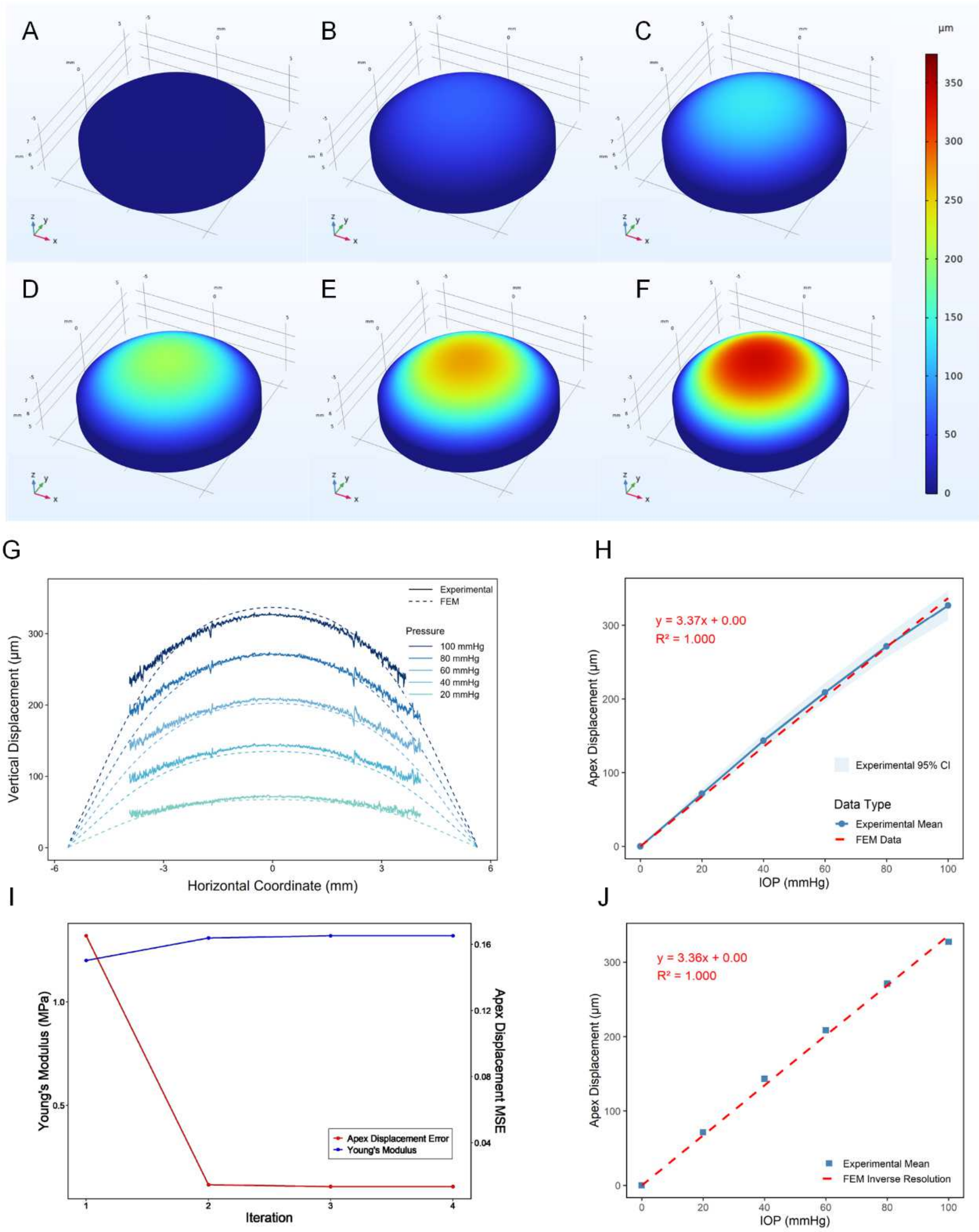

Fig. 9. Results of forward prediction and inverse parameter identification in corneal inflation experiments using the FEM method, (A–F) FEM-predicted corneal surface displacements under varying IOP of 0, 20, 40, 60, 80, and 100 mmHg, respectively, (G) Comparison of FEM-simulated and experimentally measured axial displacements on the corneal surface, (H) Comparison of simulated and measured apex displacements; blue dots represent the mean of six measurements, blue shaded area indicates the 95% confidence interval, and the red dashed line shows FEM predictions, (I) Inverse identification of the Young's modulus based on the measured mean apex displacement using a least-squares approach; convergence was achieved within two iterations, yielding a modulus of 1316.9 kPa, with a relative error of ~0.3% compared to the ground truth value of 1312.6 kPa shown in Fig. 7B, (J) Comparison between the inverse-predicted and measured apex displacement slope; the estimated value is 3.36 μm/mmHg, differing by 2.1% from the true value of 3.29 μm/mmHg.

Figure 9I presents the inverse problem solution for corneal Young's modulus identification. The Levenberg-Marquardt optimization algorithm was employed to iteratively determine the Young's modulus by minimizing the apex displacement residuals (least squares method). The red curve illustrates the least squares error of apex displacement, while the blue curve shows the corresponding Young's modulus during iteration. Results demonstrate that the optimization algorithm converged after only two iterations, yielding a final predicted Young's modulus of 1316.9 kPa. Compared with the preset true value (1312.8 kPa) in Fig. 7B, this represents a mere 0.3% relative error, confirming both the accuracy and efficiency of this inverse identification approach.

Figure 9J further demonstrates the comparison between the apex displacement obtained through FEM inverse analysis and the experimental mean values. The linear regression slope was 3.36 μm/mmHg, showing a 2.1% error compared to the experimental value of 3.29 μm/mmHg. This result validates the feasibility and accuracy of the FEM method in solving inverse problems.

4. Discussion

This study systematically compares the performance and applicability of the PIGGN and the FEM in predicting forward mechanical responses and identifying inverse mechanical parameters in artificial corneal inflation experiments. As shown in Fig. 8 and 9, both methods demonstrate the ability to accurately simulate corneal deformation under varying IOP conditions and exhibit strong potential for parameter inversion. However, significant differences exist between the two approaches in terms of methodological characteristics, prediction accuracy, convergence speed, and practical applicability, warranting further investigation.

Firstly, in terms of forward problem modeling, the conventional FEM builds on classical continuum mechanics and variational principles to formulate partial differential governing equations. Through mesh discretization and iterative numerical solutions, FEM achieves high-accuracy predictions of complex tissue deformation behavior. As illustrated in Fig. 9A–F and 9G–H, FEM successfully reproduces the radially decreasing displacement pattern from the corneal apex to the periphery under various IOP levels. Notably, the simulation results in the central region show excellent agreement with experimental measurements, with an apex displacement prediction error of only 2.1%. In contrast, although the proposed PIGGN-based method also demonstrates strong predictive capability in the central region (Fig. 8A–F), its fitting accuracy in the peripheral regions is comparatively lower.

Secondly, in the inverse problem of mechanical parameter identification, PIGGN exhibits good convergence and stability. As shown in Fig. 8I, the network converges rapidly within approximately 1200 iterations, successfully recovering the Lamé parameters λ and μ, from which a Young's modulus of 1315.2 kPa and a Poisson's ratio of 0.49 are derived, Those values highly consistent with the experimental settings. In contrast, although the FEM-based error minimization strategy achieves a near-true Young's modulus (1316.9 kPa) in just two iterations (Fig. 9I), its performance heavily relies on a well-defined model structure, accurate boundary conditions, and appropriately chosen initial parameters. Moreover, the stability and scalability of FEM are limited when addressing inverse problems involving high-dimensional and multi-parameter spaces. It is worth emphasizing that the FEM approach in this study was limited to the inversion of a single parameter (i.e., Young's modulus), whereas PIGGN, with its end-to-end deep learning framework, is capable of simultaneously identifying multiple mechanical parameters. This capability allows it to maintain high accuracy and stability even under complex boundary conditions or when high-quality initial guesses are unavailable. Such advantages present a significant opportunity for future applications in spatially-resolved elasticity imaging of non-uniform and heterogeneous biological tissues. The mechanical properties of the human cornea exhibit notable spatial heterogeneity, which poses a challenge for conventional FEM to model and invert effectively. In contrast, PINNs, such as PIGGN, naturally integrate spatial coordinates with physical constraints, enabling pointwise identification of distributed parameter fields and achieving high-resolution, noninvasive, and personalized 3D elastography. In summary, PIGGN is not only suitable for current single-point or equivalent parameter inversion tasks but also demonstrates unique potential for extension to multi-parameter, multi-scale, and even time-dependent mechanical property imaging. It thus holds promise as a foundational tool for next-generation biomechanical modeling and imaging.

It is worth noting that despite the notable advantages of PIGGN in mechanical parameter inversion, its practical application still faces challenges such as high computational resource consumption and prolonged training time. Specifically, the predictive accuracy of PIGGN is largely dependent on the density of spatial sampling point. Finer spatial "meshing" typically yields more accurate results, but also significantly increases computational costs during model training. To address this, future research could explore methods for enhancing field representation efficiency (e.g., 3D Gaussian splatting [28]), thereby advancing the applicability of PINN-based method in complex physiological scenarios such as spatially distributed mechanical property estimation (e.g., local Young's modulus reconstruction) and 3D elastography, while also validating their practical performance.

5. Conclusion

This study addresses the mechanical modeling problem in artificial corneal inflation experiments by proposing a PINN-based approach. The method enables forward prediction of the corneal three-dimensional deformation under varying IOP conditions, as well as inverse identification of mechanical parameters. A systematic comparison with the conventional FEM was also conducted. The results demonstrate that:

In terms of forward modeling, both methods accurately predict the displacement distribution of the corneal under various IOP conditions. In particular, the predictions in the central region show excellent agreement with experimental measurements, confirming the validity of the model construction and the reliability of its predictive performance.

In the inverse problem, both PIGGN and FEM successfully identified the Young's modulus, with relative errors of 0.3% and 0.2%, respectively. Notably, PIGGN is also capable of simultaneously inverting the Poisson's ratio, demonstrating strong scalability and stability in multi-parameter inversion tasks. This highlights its potential for future applications in full-field elasticity imaging inversion.

While the proposed PIGGN framework demonstrates high accuracy and efficiency for linear, homogeneous, and isotropic materials—as validated by the PDMS corneal phantoms in this study—we acknowledge that its direct application to real human corneas is currently limited. Biological corneas are inherently complex structures characterized by spatial heterogeneity, pronounced anisotropy, and nonlinear hyperelastic behavior under physiological loads. Therefore, the current linear elastic formulation serves as a foundational proof-of-concept. To bridge the gap toward clinical and biological applicability, our future work will focus on extending the weak formulation and physics-informed loss function to incorporate nonlinear hyperelastic constitutive laws (e.g., multi-parameter structural models) to accurately capture the complex biomechanics of in vivo corneal tissues.

In conclusion, this study demonstrates that PINNs can serve as a powerful complement to traditional FEM, showing great potential in tasks such as corneal mechanical behavior simulation and mechanical parameter identification.

Author Contributions

Y. Zhang designed and performed the experiments, conducted data acquisition, and implemented the numerical analysis model. Z. Gao and Z. Zhou assisted with the experiments and contributed to the experimental setup. X. Lv and X. Liu supervised the experiments and provided critical feedback. T. Quan provided methodological guidance on the numerical analysis. H. Wang and S. Zeng conceived and designed the study, and guided the research framework and manuscript organization. All authors contributed to writing, discussed the results, reviewed, and approved the final version of the manuscript.

Acknowledgement

Not applicable.

Conflict of Interest

The authors declared that they have no conflicts of interest to this work.

Funding

This work was supported by the National Natural Science Foundation of China (Grant No. 62275094), the National Key Research and Development Program of China (Grant No. 2022YFC2404500), and the Postdoctoral Elite Talent Introduction Program of Hubei Province (Grant No. 2024HBBHJD030).

Data Availability Statements

No human or animal subjects were involved in the research. All numerical simulations and machine learning analyses were performed using synthetic data derived from controlled laboratory measurements. The study did not require institutional ethics review as it did not involve biological specimens or clinical data.

Reference

[1] Ruberti, J.W., Sinha Roy, A., Roberts, C.J., Corneal biomechanics and biomaterials, *Annual Review of Biomedical Engineering*, 13(1), 2011, 269-295.
[2] Ávila, F.J., Marcellán, M.C., Remón, L., On the relationship between corneal biomechanics, macrostructure, and optical properties, *Journal of Imaging*, 7(12), 2021, 280.
[3] Wilson, A., Marshall, J., A review of corneal biomechanics: Mechanisms for measurement and the implications for refractive surgery, *Indian Journal of Ophthalmology*, 68(12), 2020, 2679-2690.
[4] Wen, J., Chen, X., Yang, Y., Liu, J., Li, E., Liu, J., Zhou, Z., Wu, W., He, K., Acupuncture Medical Therapy and its Underlying Mechanisms: A Systematic Review, *American Journal of Chinese Medicine*, 49(1), 2021, 1-23.
[5] Matteoli, S., Virga, A., Paladini, I., Mencucci, R., Corvi, A., Investigation into the Elastic Properties of ex vivo Porcine Corneas Subjected to Inflation Test after Cross-Linking Treatment, *Journal of Applied Biomaterials & Functional Materials*, 14(2), 2016, 163-170.
[6] Wang, L., Tian, L., Huang, Y., Huang, Y., Zheng, Y., Assessment of corneal biomechanical properties with inflation test using optical coherence tomography, *Annals of Biomedical Engineering*, 46(2), 2018, 247-256.
[7] Chang, S.H., Zhou, D., Eliasy, A., Li, Y.C., Elsheikh, A., Experimental evaluation of stiffening effect induced by UVA/Riboflavin corneal cross-linking using intact porcine eye globes, *PLoS One*, 15(11), 2020, e0240724.
[8] Piñero, D.P., Alcón, N., Corneal biomechanics: a review, *Clinical and Experimental Optometry*, 98(2), 2015, 107-116.
[9] Zhou, Z., Wang, H., Zhang, Y., Lv, H., Zhang, Z., Li, H., Liu, X., Quan, T., Lv, X., Zeng, S., Biomechanical Characterization of Central Corneal Region Using Inflation Test and its Application to Predicting Central Corneal Response Under Intraocular Pressure, *Annals of Biomedical Engineering*, 54(1), 2016, 303-315.
[10] Zhou, Z., Wang, H., Wang, Z., Zhang, Y., Lv, H., Zhang, Z., Gao, Z., Liu, X., Lv, X., Quan, T., Chen, S., Non-invasive measurement of in vivo corneal steady-state biomechanical properties via controllable negative pressure inflation, *IEEE Transactions on Biomedical Engineering*, 73, 2025, 1289-1297.
[11] Lv, H., Zhou, Z., Qu, Y., Zhang, Z., Zhang, Y., Zhang, H., Wu, H., Zhao, D., Wang, Z., Lu, J., Wang, H., Measurement Device for Corneal Static Biomechanical Properties Based on Negative Pressure Adhesion, *IEEE Transactions on Instrumentation and Measurement*, 74, 2025, 4015006.
[12] Bao, F., Wang, J., Cao, S., Liao, N., Shu, B., Zhao, Y., Li, Y., Zheng, X., Huang, J., Chen, S., Wang, Q., Development and clinical verification of numerical simulation for laser in situ keratomileusis, *Journal of the Mechanical Behavior of Biomedical Materials*, 83, 2018, 126-134.
[13] Quan, T., Zhou, Z., Zhang, Z., Wei, Y., Feng, X., Liu, X., Lv, X., Zeng, S., Wang, H., Model control of corneal surface curvature during refractive surgery: validation on artificial eyes, 2024, DOI: 10.1364/opticaopen.26778595.v1.
[14] Zheng, X., Bao, F., Geraghty, B., Huang, J., Yu, A., Wang, Q., High intercorneal symmetry in corneal biomechanical metrics, *Eye and Vision*, 3(1), 2016, 7.
[15] Bao, F., Deng, M., Zheng, X., Li, L., Zhao, Y., Cao, S., Yu, A., Wang, Q., Huang, J., Elsheikh, A., Effects of diabetes mellitus on biomechanical properties of the rabbit cornea, *Experimental Eye Research*, 161, 2017, 82-88.
[16] Soize, C., An overview on uncertainty quantification and probabilistic learning on manifolds in multiscale mechanics of materials, *Mathematics and Mechanics of Complex Systems*, 11(1), 2023, 87-174.
[17] dell'Isola, F., D'Annibale, F., Luciano, R., Henze, T., Giorgio, I., A generalised plate with kinematically independent thickness for modelling shapes of corneas affected by keratoconus before and after penetrating keratoplasty, *Mathematics and Mechanics of Solids*, 2025, DOI: 10.1177/10812865251345814.
[18] Mazinani, P., Cardillo, C., Shear wave velocity and finite element modeling for understanding keratoconus biomechanics: Comparison with healthy cornea, *Mathematics and Mechanics of Solids*, 2025, DOI: 10.1177/10812865251347512.
[19] Yin, Z., Li, G.Y., Zhang, Z., Zheng, Y., Cao, Y., SWENet: A physics-informed deep neural network (PINN) for shear wave elastography, *IEEE Transactions on Medical Imaging*, 43(4), 2023, 1434-1448.
[20] Kamali, A., Sarabian, M., Laksari, K., Elasticity imaging using physics-informed neural networks: Spatial discovery of elastic modulus and Poisson's ratio, *Acta Biomaterialia*, 155, 2023, 400-409.
[21] Ragoza, M., Batmanghelich, K., Physics-informed neural networks for tissue elasticity reconstruction in magnetic resonance elastography, *International Conference on Medical Image Computing and Computer-Assisted Intervention*, 2023, 333-343
[22] Zhang, Y., Liao, J., Feng, Z., Yang, W., Perelli, A., Wang, Z., Li, C., Huang, Z., VP-net: an end-to-end deep learning network for elastic wave velocity prediction in human skin in vivo using optical coherence elastography, *Frontiers in Bioengineering and Biotechnology*, 12, 2024, 1465823.
[23] Gao, H., Zahr, M.J., Wang, J.X., Physics-informed graph neural Galerkin networks: A unified framework for solving PDE-governed forward and inverse problems, *Computer Methods in Applied Mechanics and Engineering*, 390, 2022, 114502.
[24] Cho, H.S., Jeoung, S.C., Yang, Y.S., Development of eye phantom for mimicking the deformation of the human cornea accompanied by intraocular pressure alterations, *Scientific Reports*, 12(1), 2022, 20670.
[25] Pandolfi, A., Manganiello, F., A model for the human cornea: constitutive formulation and numerical analysis, *Biomechanics and Modeling in Mechanobiology*, 5(4), 2006, 237-246.
[26] Defferrard, M., Bresson, X., Vandergheynst, P., Convolutional neural networks on graphs with fast localized spectral filtering, *Advances in Neural Information Processing Systems*, 29, 2016.
[27] Bower, A.F., *Applied mechanics of solids (Chapter 5)*, CRC Press, 2010.
[28] Kerbl, B., Kopanas, G., Leimkühler, T., Drettakis, G., 3d gaussian splatting for real-time radiance field rendering, *ACM Transactions on Graphics*, 42(4),

2023, 139.
[29] Clayson, K., Pavlatos, E., Ma, Y., Liu, J., 3D Characterization of corneal deformation using ultrasound speckle tracking, *Journal of Innovative Optical Health Sciences*, 10(06), 2017, 1742005.
[30] Kingma, D.P., Ba, J., Adam: A method for stochastic optimization, *arXiv preprint*, arXiv:1412.6980, 2014.

ORCID iD

Ying Zhang https://orcid.org/0009-0005-8984-8503
Honghao Wang https://orcid.org/0000-0002-1622-0417

How to cite this article: Zhang Y., et al., Physics-Informed Neural Network Modeling of Corneal Inflation: Forward Prediction and Inverse Parameter Identification, *J. Appl. Comput. Mech.*, xx(x), 2026, 1–14. https://doi.org/10.22055/jacm.2026.49003.5659